

Steady Rayleigh–Bénard convection between stress-free boundaries

Baole Wen¹†, David Goluskin², Matthew LeDuc³,
Gregory P. Chini^{4,5}, and Charles R. Doering^{1,3,6}

¹Department of Mathematics, University of Michigan, Ann Arbor MI 48109-1043

²Department of Mathematics & Statistics, University of Victoria, Victoria, BC V8P 5C2

³Department of Physics, University of Michigan, Ann Arbor, MI 48109-1040

⁴Program in Integrated Applied Mathematics, University of New Hampshire, Durham NH 03824

⁵Department of Mechanical Engineering, University of New Hampshire, Durham NH 03824

⁶Center for the Study of Complex Systems, University of Michigan, Ann Arbor MI 48109-1042

(Received xx; revised xx; accepted xx)

Steady two-dimensional Rayleigh–Bénard convection between stress-free isothermal boundaries is studied via numerical computations. We explore properties of steady convective rolls with aspect ratios $\pi/5 \leq \Gamma \leq 4\pi$, where Γ is the width-to-height ratio for a pair of counter-rotating rolls, over eight orders of magnitude in the Rayleigh number, $10^3 \leq Ra \leq 10^{11}$, and four orders of magnitude in the Prandtl number, $10^{-2} \leq Pr \leq 10^2$. At large Ra where steady rolls are dynamically unstable, the computed rolls display $Ra \rightarrow \infty$ asymptotic scaling. In this regime, the Nusselt number Nu that measures heat transport scales as $Ra^{1/3}$ uniformly in Pr . The prefactor of this scaling depends on Γ and is largest at $\Gamma \approx 1.9$. The Reynolds number Re for large- Ra rolls scales as $Pr^{-1}Ra^{2/3}$ with a prefactor that is largest at $\Gamma \approx 4.5$. All of these large- Ra features agree quantitatively with the semi-analytical asymptotic solutions constructed by Chini & Cox (2009). Convergence of Nu and Re to their asymptotic scalings occurs more slowly when Pr is larger and when Γ is smaller.

Key words: convection, coherent structure, heat transport

1. Introduction

Natural convection is the buoyancy-driven flow resulting from unstable density variations, typically due to thermal or compositional inhomogeneities, in the presence of a gravitational field. It remains the focus of experimental, computational, and theoretical research worldwide, in large part because buoyancy-driven flows are central to engineering heat transport, atmosphere and ocean dynamics, climate science, geodynamics, and stellar physics. Rayleigh–Bénard convection, in which a layer of fluid is confined between isothermal horizontal boundaries with the higher temperature on the underside (Rayleigh 1916) is studied extensively as a relatively simple system displaying the essential phenomena. Beyond the importance of buoyancy-driven flow in applications, Rayleigh’s model has served for more than a century as a primary paradigm of nonlinear physics (Malkus &

† Email address for correspondence: baolew@umich.edu

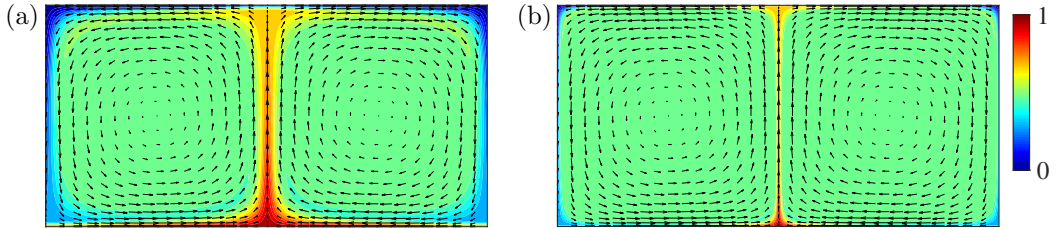


Figure 1: Steady convective rolls between stress-free boundaries for (a) $Ra = 10^6$ and (b) $Ra = 10^8$, with $Pr = 1$ and a horizontal period that is twice the layer height. Color represents dimensionless temperature and arrows indicate the velocity vector field. As $Ra \rightarrow \infty$, the temperature field develops an isothermal core while the thermal boundary layers and plumes become thinner and the velocity field converges to a Ra -independent pattern that lacks boundary layers.

Veronis 1958), complex dynamics (Lorenz 1963), pattern formation (Newell & Whitehead 1969), and turbulence (Kadanoff 2001).

A central feature of Rayleigh–Bénard convection is the Nusselt number Nu , the factor by which convection enhances heat transport relative to conduction alone. A fundamental challenge for the field is to understand how Nu depends on the dimensionless control parameters: the Rayleigh number Ra , which is proportional to the imposed temperature difference across the layer, the fluid’s Prandtl number Pr , and geometric parameters like the domain’s width-to-height aspect ratio Γ . Rayleigh (1916) studied the bifurcation from the static conduction state (where $Nu = 1$) to convection (where $Nu > 1$) when Ra exceeds a Pr -independent finite value. In the strongly nonlinear large- Ra regime relevant to many applications, convective turbulence is characterized by chaotic plumes that emerge from thin thermal boundary layers and stir a statistically well-mixed bulk. Power-law behavior where Nu scales like $Pr^\beta Ra^\gamma$ is often presumed for heat transport in the turbulent regime, but heuristic theories—i.e., physical arguments relying on uncontrolled approximations—yield various predictions for the scaling exponents. Rigorous upper bounds on Nu derived from the equations of motion place restrictions on possible asymptotic exponents but do not imply unique values. Meanwhile, direct numerical simulations (DNS) and laboratory experiments designed to respect the approximations employed in Rayleigh’s model have produced extensive data on Nu over wide ranges of Ra , Pr , and Γ . Even so, consensus regarding the asymptotic large- Ra behavior of Nu remains to be achieved (Chillà & Schumacher 2012; Doering 2020).

In addition to the turbulent convection generally observed at large Ra , there are much simpler steady solutions to the equations of motion such as the pair of steady counter-rotating rolls shown in figure 1. Steady coherent flows are not typically seen in large- Ra simulations or experiments because they are dynamically unstable. Nonetheless, they are part of the global attractor for the infinite-dimensional dynamical system defined by Rayleigh’s model, and recent results suggest that steady rolls may be one of the key coherent states comprising the ‘backbone’ of turbulent convection. In the case of no-slip top and bottom boundaries Waleffe *et al.* (2015) and Sondak *et al.* (2015) found that, over the range of Rayleigh numbers they explored, two-dimensional (2D) steady rolls display Nu values very close to those of three-dimensional (3D) convective turbulence, provided that the horizontal period of the rolls is tuned to maximize Nu at each value of Ra .

Here we report computations of steady 2D convective rolls in the case of stress-free top and bottom boundaries. We have carried out computations using spectral methods over eight orders of magnitude in Ra , four orders of magnitude in Pr , and more than an order of magnitude in the aspect ratio Γ , defined as the width-to-height ratio of a pair of rolls. As in the no-slip case, our steady states share many features with time-dependent simulations between stress-free boundaries (Paul *et al.* 2012; Wang *et al.* 2020). Moreover, the results verify predictions about the $Ra \rightarrow \infty$ limit made by Chini & Cox (2009) who extended an approach initiated by Robinson (1967) to construct matched asymptotic approximations of steady rolls between stress-free boundaries. In particular, our computations agree quantitatively with the asymptotic prediction that $Nu = \mathcal{O}(Ra^{1/3})$ uniformly in Pr with a Γ -dependent prefactor that assumes its maximum value at $\Gamma \approx 1.9$, and with corresponding asymptotic predictions about the Reynolds number that are derived in the Appendix. The rest of this paper is organized as follows. The equations governing Rayleigh–Bénard convection and our numerical scheme for computing steady solutions are outlined in §2. The computational results are presented in §3, followed by further discussion in §4.

2. Governing equations and computational methods

The Boussinesq approximation to the Navier–Stokes equations used by Rayleigh (1916) to model convection in a 2D fluid layer are, in dimensionless variables,

$$\partial_t \mathbf{u} + \mathbf{u} \cdot \nabla \mathbf{u} = -\nabla p + Pr \nabla^2 \mathbf{u} + Pr Ra T \hat{\mathbf{z}}, \quad (2.1a)$$

$$\nabla \cdot \mathbf{u} = 0, \quad (2.1b)$$

$$\partial_t T + \mathbf{u} \cdot \nabla T = \nabla^2 T, \quad (2.1c)$$

where $\mathbf{u} = u\hat{\mathbf{x}} + w\hat{\mathbf{z}}$ is the velocity, p is the pressure, and T is the temperature. The system has been nondimensionalized using the layer thickness h , the thermal diffusion time h^2/κ , where κ is the thermal diffusivity, and the temperature drop Δ from the bottom boundary to the top one.

The dimensionless spatial domain is $(x, z) \in [0, \Gamma] \times [0, 1]$, and all dependent variables are taken to be Γ -periodic in x . At the lower ($z = 0$) and upper ($z = 1$) boundaries, the temperature satisfies isothermal conditions while the velocity field satisfies no-penetration and stress-free boundary conditions:

$$T|_{z=0} = 1 \text{ and } T|_{z=1} = 0, \quad w|_{z=0,1} = 0, \quad \partial_z u|_{z=0,1} = 0. \quad (2.2)$$

The three dimensionless parameters of the problem are the aspect ratio Γ , the Prandtl number $Pr = \nu/\kappa$, where ν is the kinematic viscosity, and the Rayleigh number $Ra = g\alpha\Delta h^3/\nu\kappa$, where $-g\hat{\mathbf{z}}$ is the gravitational acceleration vector and α is the thermal expansion coefficient. A single pair of the steady rolls computed here fits in the domain, meaning the aspect ratio of the pair is Γ while that of each individual roll is $\Gamma/2$.

The static conduction state, for which $\mathbf{u} = \mathbf{0}$ and $T = 1 - z$, solves (2.1) and (2.2) at all parameter values. Rayleigh (1916) showed that rolls vertically spanning the layer with aspect ratio Γ bifurcate supercritically from the conduction state as Ra increases past

$$Ra_c(k) = \frac{(k^2 + \pi^2)^3}{k^2}, \quad (2.3)$$

where $k = 2\pi/\Gamma$ is the wavenumber of the fundamental period of the domain. The conduction state is absolutely stable if $Ra < Ra_c(k)$ for all k admitted by the domain; see, e.g., Goluskin (2015).

The Nusselt number is defined as the ratio of total mean heat flux in the vertical direction to the flux from conduction alone:

$$Nu = 1 + \langle wT \rangle, \quad (2.4)$$

where w and T are dimensionless solutions of (2.1) and $\langle \cdot \rangle$ indicates an average over space and infinite time. (For steady states the time average is not needed.) The governing equations imply the equivalent expressions

$$Nu = \langle |\nabla T|^2 \rangle = 1 + \frac{1}{Ra} \langle |\nabla u|^2 + |\nabla w|^2 \rangle, \quad (2.5)$$

the latter of which self-evidently ensures $Nu > 1$ for all sustained convection. Another emergent measure of the intensity of convection is the bulk Reynolds number defined using the dimensional root-mean-squared velocity U_{rms} , which in terms of dimensional quantities is $Re = U_{rms}h/\nu$. We choose our reference frame such that $\langle u \rangle = 0$, so in dimensionless terms

$$Re = \frac{1}{Pr} \langle u^2 + w^2 \rangle^{1/2}. \quad (2.6)$$

We compute steady ($\partial_t = 0$) solutions of (2.1) using a vorticity–stream function formulation,

$$\partial_z \psi \partial_x \omega - \partial_x \psi \partial_z \omega = Pr \nabla^2 \omega + Pr Ra \partial_x \theta, \quad (2.7a)$$

$$\nabla^2 \psi = -\omega, \quad (2.7b)$$

$$\partial_z \psi \partial_x \theta - \partial_x \psi \partial_z \theta = -\partial_x \psi + \nabla^2 \theta, \quad (2.7c)$$

where the stream function ψ is defined by $\mathbf{u} = \hat{\mathbf{x}}\partial_z \psi - \hat{\mathbf{z}}\partial_x \psi$, the (negative) scalar vorticity is $\omega = \partial_x w - \partial_z u = -\nabla^2 \psi$, and θ is the deviation of the temperature field T from the conduction profile $1 - z$. The boundary conditions used in our computations are that ψ , $\nabla^2 \psi$, and θ vanish on both boundaries. The latter two conditions follow from the stress-free and fixed-temperature conditions, respectively. Impenetrability of the boundaries implies that ψ is constant on each boundary, and choosing the reference frame where $\langle u \rangle = 0$ requires these constants to be identical. Their value can be fixed to zero since translating ψ by a constant does not affect the dynamics.

We solve the time-independent equations (2.7) numerically using a Newton–GMRES (generalised minimal residual) iterative scheme. Starting with an initial iterate $(\omega^0, \psi^0, \theta^0)$ that does not exactly solve (2.7), each iteration of the Newton’s method applies a correction until the resulting iterates have converged to a solution of (2.7). Following Wen *et al.* (2015b) and Wen & Chini (2018), the linear partial differential equations for the corrections are

$$(Pr \nabla^2 - \psi_z \partial_x + \psi_x \partial_z)^i \Delta \omega + (-\omega_x \partial_z + \omega_z \partial_x)^i \Delta \psi + Ra Pr \partial_x \Delta \theta = -F_{res}^{\omega^i}, \quad (2.8a)$$

$$\Delta \omega + \nabla^2 \Delta \psi = -F_{res}^{\psi^i}, \quad (2.8b)$$

$$(-\partial_x + \theta_z \partial_x - \theta_x \partial_z)^i \Delta \psi + (\nabla^2 - \psi_z \partial_x + \psi_x \partial_z)^i \Delta \theta = -F_{res}^{\theta^i}, \quad (2.8c)$$

where the superscript i denotes the i^{th} Newton iterate, the corrections are defined as

$$\Delta \omega = \omega^{i+1} - \omega^i, \quad \Delta \psi = \psi^{i+1} - \psi^i, \quad \Delta \theta = \theta^{i+1} - \theta^i \quad (2.9)$$

and vanish on the boundaries, and

$$F_{res}^\omega = Pr\nabla^2\omega + RaPr\theta_x - \psi_z\omega_x + \psi_x\omega_z, \quad (2.10a)$$

$$F_{res}^\psi = \nabla^2\psi + \omega, \quad (2.10b)$$

$$F_{res}^\theta = \nabla^2\theta - (\psi_z\theta_x - \psi_x\theta_z + \psi_x) \quad (2.10c)$$

are the residuals of the nonlinear steady equations (2.7). We simplify the implementation by setting $F_{res}^\psi = 0$, in which case Δ^ψ can be obtained by solving $\nabla^2\Delta^\psi = -\Delta^\omega$ for a given Δ^ω . After this simplification, the pair (2.8a) and (2.8c) can be solved simultaneously for Δ^ω and Δ^θ .

For each iteration of Newton’s method, we solve (2.8a) and (2.8c) iteratively using the GMRES method (Trefethen & Bau III 1997). The spatial discretization is spectral, using a Fourier series in x and a Chebyshev collocation method in z (Trefethen 2000). The ∇^2 operator is used as a preconditioner to accelerate convergence of the GMRES iterations. The roll states of interest have centro-reflection symmetries (cf. figure 1),

$$[\omega, \psi, \theta](x, z) = [\omega, \psi, -\theta](\Gamma/2 - x, 1 - z), \quad [\omega, \psi, \theta](x, z) = [-\omega, -\psi, \theta](\Gamma - x, z), \quad (2.11)$$

which allow the full fields to be recovered from their values on one quarter of the domain, so we encode these symmetries to reduce the number of unknowns. The GMRES iterations are stopped once the L^2 -norm of the relative residual of (2.8a, c) is less than 10^{-2} , and the Newton iterations are stopped once the L^2 -norm of the relative residual of (2.7a, c) is less than 10^{-10} . For Ra not far above the critical value $Ra_c(k)$, convergence to rolls of period $\Gamma = 2\pi/k$ is accomplished by choosing the initial iterate with $\omega^0 = -\sqrt{RaPr}\sin(\pi z)\sin(kx)$ and $\theta^0 = -0.1[\sin(2\pi z) + \sin(\pi z)\cos(kx)]$. For each Pr , results from smaller Ra (or Γ) are used as the initial iterate for larger Ra (or Γ).

3. Results

We computed steady rolls over a wide range of Ra starting just above the value $Ra_c(k)$ at which the rolls bifurcate from the conduction state and ranging up to 10^9 or higher depending on the other parameters. Computations were carried out for $Pr = 10^{-2}, 10^{-1}, 1, 10, 10^2$ and a range of values of Γ such that the fundamental wavenumber $k = 2\pi/\Gamma$ lies in $1/2 \leq k \leq 10$. Data for all the $\Gamma = 2$ cases are tabulated in the Supplementary Material.

Our computations reach sufficiently large Ra to show clear asymptotic scalings of bulk quantities:

$$Nu \sim c_n(k)Ra^{1/3} \quad \text{and} \quad Re \sim c_r(k)Pr^{-1}Ra^{2/3} \quad \text{as} \quad Ra \rightarrow \infty. \quad (3.1)$$

Both of these scalings are predicted by the asymptotic analysis of Chini & Cox (2009), although only the Nu scaling was stated explicitly there. Chini & Cox gave an asymptotic prediction for the prefactor $c_n(k)$ but not for $c_r(k)$. Using their asymptotic approximations for the stream function and vorticity within each convection roll, we derived an expression for $c_r(k)$ in terms of $c_n(k)$ that is presented in the Appendix.

Figure 2 shows the Ra -dependence of the compensated quantities $Nu/Ra^{1/3}$ and $RePr/Ra^{2/3}$ for rolls of aspect ratio $\Gamma = 2$ ($k = \pi$) at various Pr . Rolls of this aspect ratio bifurcate from the conduction state at the Rayleigh number $Ra_c(\pi) = 8\pi^4 \approx 779$. It is clear from figure 2 that both Nu and the Péclet number $RePr$ become independent of Pr as $Ra \rightarrow \infty$, as predicted by the asymptotics of Chini & Cox (2009), and also as Ra decreases towards the Pr -independent value Ra_c . Convergence to the large- Ra asymptotic scaling is slower when Pr is larger, at least over the four decades of Pr

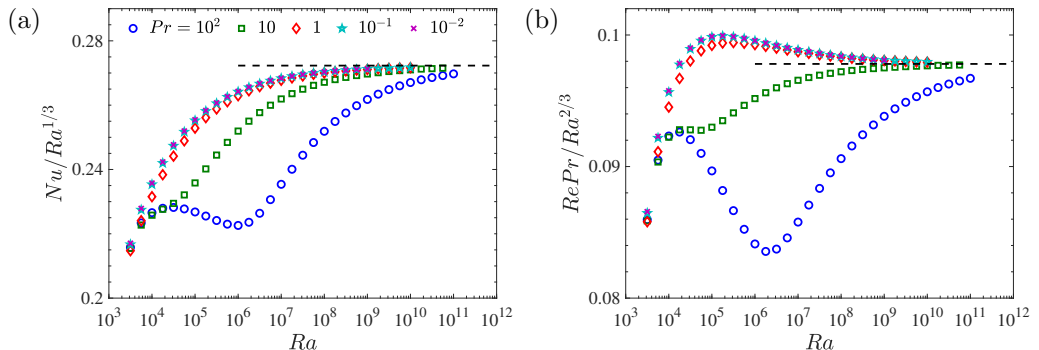


Figure 2: The Ra -dependence of (a) Nu and (b) Re , compensated by the asymptotic scalings (3.1), for steady convective rolls with $\Gamma = 2$ ($k = \pi$) at various Pr . Dashed lines in panels (a) and (b) denote, respectively, the asymptotic prefactor $c_n(\pi) \approx 0.2723$ from Chini & Cox (2009) and our asymptotic prediction $c_r(\pi) \approx 0.0978$. Figure 6 shows the same Nu values *not* compensated by $Ra^{1/3}$.

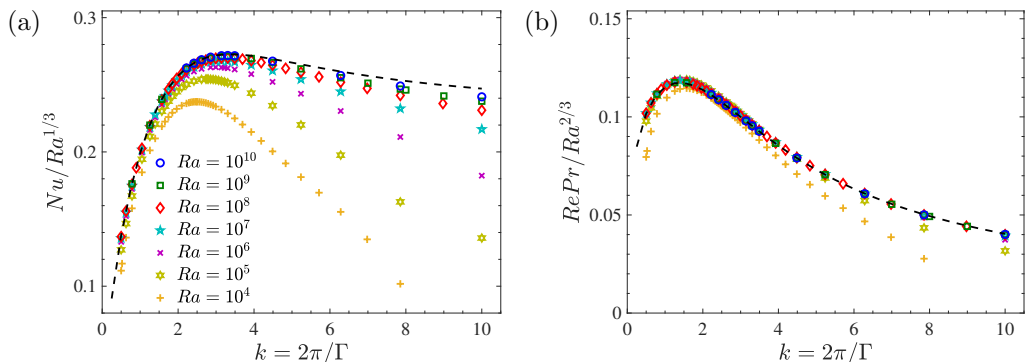


Figure 3: The k -dependence of (a) Nu and (b) Re , compensated by the asymptotic scalings (3.1), for steady convective rolls with $Pr = 1$ at various Ra . The dashed lines in panels (a) and (b) are, respectively, the asymptotic prefactor $c_n(k)$ predicted by Chini & Cox (2009) and the corresponding prefactor $c_r(k)$ we derived using their results.

considered here. Numerical values of Nu and Re at large Ra suggest scaling prefactors that are indistinguishable from the values $c_n(\pi) \approx 0.2723$ and $c_r(\pi) \approx 0.0978$ predicted by asymptotic analysis.

Nusselt and Reynolds numbers of steady rolls converge to the asymptotic scalings (3.1) over the full range $1/2 \leq k \leq 10$ for which we have computed steady rolls. This is evident in figure 3 where the k -dependence of the compensated quantities $Nu/Ra^{1/3}$ and $RePr/Ra^{2/3}$ is shown for various Ra in the $Pr = 1$ case. As Ra increases these quantities converge to asymptotic curves that we have called $c_n(k)$ and $c_r(k)$. It is clear from the figure that this convergence is slower when k is larger, and that Re reaches its asymptotic scaling sooner than Nu does. Since rolls with $k = \pi/\sqrt{2}$ are the first to bifurcate from the conduction state, at $Ra_c(\pi/\sqrt{2}) = 27\pi^4/4$, this is the k that initially maximizes both Nu and Re . As $Ra \rightarrow \infty$, the k values that maximize Nu and Re approach the asymptotic

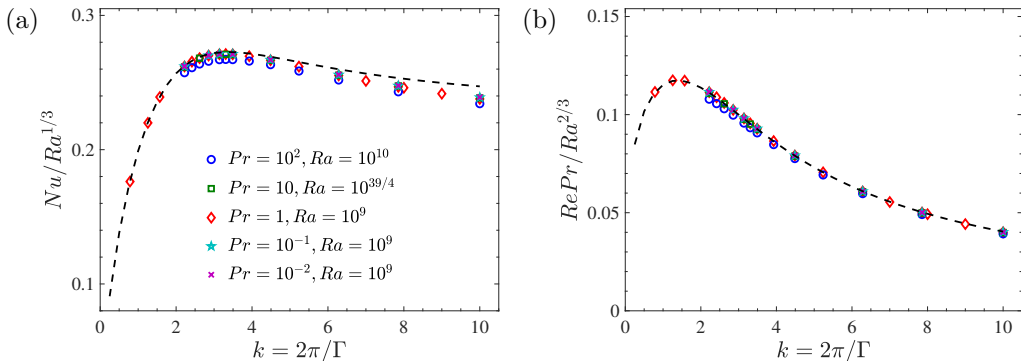


Figure 4: Dependence of compensated (a) Nu and (b) Re on k for various Pr in the large- Ra asymptotic regime. Reaching this regime requires larger Ra when Pr is larger. Asymptotic predictions (---) of $c_n(k)$ and $c_r(k)$ are as in figure 3.

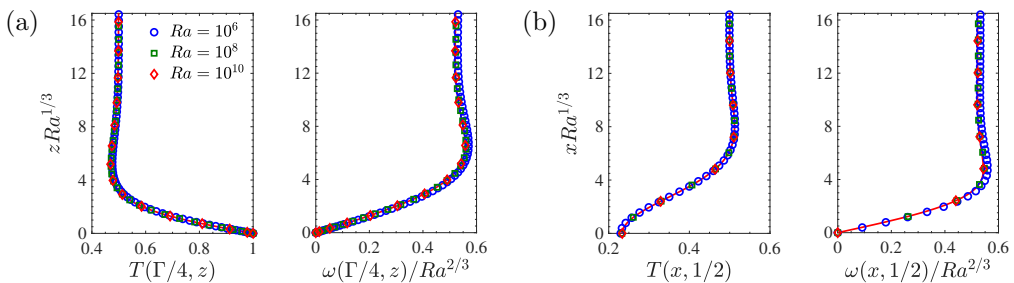


Figure 5: Scaled spatial structure of temperature T and compensated vorticity ω near the (a) bottom and (b) left side of a convection roll where $Pr = 1$ and $\Gamma = 2$. Solid curves are spectral interpolants of $Ra = 10^{10}$ values.

values $k \approx 3.31$ ($\Gamma \approx 1.9$) and $k \approx 1.4$ ($\Gamma \approx 4.5$), respectively, where the corresponding maximal prefactors are $c_n \approx 0.273$ and $c_r \approx 0.117$.

Both Nu and the Péclet number $RePr$ of steady rolls become nearly independent of Pr as Ra grows large. The large- Ra coalescence of data for different Pr is evident for the $k = \pi$ case in figure 2, as is the fact that Pr can have a substantial effect in the pre-asymptotic regime. To show that Pr -independence at large Ra occurs over the full range $1/2 \leq k \leq 10$ of our computations, figure 4 depicts the k -dependence of compensated Nu and Re at large Ra for various Pr . All $Nu/Ra^{1/3}$ and $RePr/Ra^{2/3}$ values plotted in figure 4 fall close to the asymptotic predictions for $c_n(k)$ and $c_r(k)$ that, at leading order in the asymptotic small parameter $Ra^{-1/3}$, are independent of Pr .

The asymptotic scaling of steady rolls at large Ra is reflected not only in the collapse of rescaled bulk quantities like $Nu/Ra^{1/3}$ and $RePr/Ra^{2/3}$ but also in the collapse of the boundary and internal layer profiles when the appropriate spatial variable is stretched by $Ra^{1/3}$. Figure 5 shows this collapse of the temperature and vorticity profiles at the bottom boundary and at the left edge of the periodic domain for the case where $Pr = 1$ and $\Gamma = 2$ ($k = \pi$). Coincidence of these scaled profiles at large Ra confirms that the thickness of both the thermal and vorticity layers scale like $Ra^{-1/3}$ on all four edges

of a single convection roll, while both fields are strongly homogenized in the interior with $T \sim 1/2$ and $\omega \sim 0.522Ra^{2/3}$. Profiles at other Pr are not shown but collapse similarly. These findings confirm the deduction of a homogenized interior by Chini & Cox (2009), as well as their prediction that the core vorticity magnitude is asymptotic to $\sqrt{c_n(\pi)}Ra^{2/3} \approx 0.5218Ra^{2/3}$ uniformly in Pr .

Another quantity of interest is the kinetic energy dissipation rate per unit mass,

$$\varepsilon(\mathbf{x}^*, t^*) = \frac{\nu}{2} \sum_{i,j=1}^2 (\partial_{x_i^*} u_j^* + \partial_{x_j^*} u_i^*)^2, \quad (3.2)$$

where $*$ denotes dimensional variables. The corresponding bulk viscous dissipation coefficient $C = \langle \varepsilon \rangle h / U_{rms}^3$ can be expressed in dimensionless variables as

$$C = Re^{-3} Pr^{-2} \left\langle \frac{1}{2} \sum_{i,j=1}^2 (\partial_i u_j + \partial_j u_i)^2 \right\rangle. \quad (3.3)$$

Identity (2.5) gives $C = Re^{-3} Pr^{-2} Ra(Nu - 1)$, so the asymptotic scalings (3.1) imply

$$C \sim c_n(k) c_r(k)^{-3} Pr Ra^{-2/3} \sim c_n(k) c_r(k)^{-2} Re^{-1}. \quad (3.4)$$

That is, C depends asymptotically on Ra and Pr via the distinguished combination $Pr Ra^{-2/3}$ that is asymptotic to Re^{-1} . This scaling of the dissipation coefficient is characteristic of flows without viscous boundary layers, such as laminar Couette or Poiseuille flow, consistent with the steady velocity fields computed here (cf. figure 1). Indeed, for stress-free steady convection, viscous dissipation is dominated by that in the homogenized core since the vorticity is of the same asymptotic magnitude in the core as in the thin vorticity layers.

The average of dissipation over time and horizontal directions, denoted $\bar{\varepsilon}(z)$, has been used to compare convection between the cases of stress-free and no-slip boundaries. In 3D simulations of the stress-free case at $Ra = 5 \times 10^6$, Petschel *et al.* (2013) found that the normalized profile $\bar{\varepsilon}(z)/\langle \varepsilon \rangle$ exhibits ‘dissipation layers’ near the boundaries that depend strongly on Pr . In steady rolls, on the other hand, we find that $\bar{\varepsilon}(z)/\langle \varepsilon \rangle$ is independent of Pr at asymptotically large Ra , as shown in figure S1 of the Supplementary Material.

4. Discussion

The steady rolls we have computed share many features with unsteady flows from DNS of Rayleigh–Bénard convection with isothermal stress-free boundary conditions. In recent simulations, Wang *et al.* (2020) found multistability between unsteady states exhibiting various numbers of roll pairs in wide 2D domains. Each of the coexisting states suggested scalings approaching the $Nu = \mathcal{O}(Ra^{1/3})$ and $Re = \mathcal{O}(Ra^{2/3})$ asymptotic behaviour of steady rolls. As in the steady case, the prefactors of these scalings depended on the mean aspect ratios of the unsteady rolls. The highest Nusselt numbers among Wang *et al.*’s data occur in five-roll-pair states in a $\Gamma = 16$ domain—meaning each roll pair has $\Gamma \approx 3.2$ on average—but steady $\Gamma = 3.2$ rolls have still larger Nu . At $Ra = 10^9$ and $Pr = 10$, for example, the DNS exhibit $Nu = 198.01$ and $Re = 10135$ while steady $\Gamma = 3.2$ rolls at the same parameters yield the larger values of $Nu = 253.61$ and $Re = 11333$, and comparisons at other Ra are similar (cf. Table S4 of the Supplementary Material). Figure 6 shows the Nu of these five-roll-pair DNS states along with the larger Nu of the steady rolls computed here for various Pr and $\Gamma = 2$. The steady rolls also achieve larger Nu values than have been attained in other unsteady simulations with stress-free boundaries in 2D

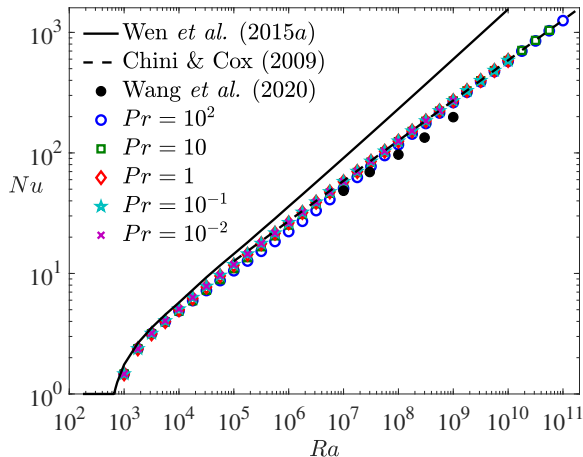


Figure 6: Dependence of Nu on Ra for: steady rolls with $\Gamma = 2$ and various Pr , time-dependent 2D simulations with mean aspect ratio $\Gamma = 3.2$ and $Pr = 10$ (Wang *et al.* 2020, see text), and upper bounds applying to all flows with $\Gamma = 2\sqrt{2}$ and any Pr (Wen *et al.* 2015*a*, see text). The dashed line is the asymptotic prediction $Nu \sim 0.2723 Ra^{1/3}$ of Chini & Cox (2009) for $\Gamma = 2$. The same Nu values of steady rolls are shown compensated by $Ra^{1/3}$ in figure 1.

(van der Poel *et al.* 2014; Goluskin *et al.* 2014) and in 3D (Petschel *et al.* 2013; Pandey *et al.* 2014; Pandey & Verma 2016; Pandey *et al.* 2016).

Comparing steady rolls in the stress-free case with those previously computed in the no-slip case, there are significant differences in their dependence on the aspect ratio Γ . With stress-free boundaries, $Nu = \mathcal{O}(Ra^{1/3})$ for each Γ as $Ra \rightarrow \infty$, with maximal asymptotic heat transport attained by rolls of optimal aspect ratio $\Gamma \approx 1.9$. In the no-slip computations of Waleffe *et al.* (2015) and Sondak *et al.* (2015), on the other hand, the Γ values that maximize Nu decrease towards zero proportionally to $Ra^{-0.22}$ at large Ra . (A similar phenomenon occurs in porous medium Rayleigh–Bénard convection; see Wen *et al.* (2015*b*).) The no-slip steady rolls display Nu scaling like $Ra^{0.28}$ when Γ is fixed but scaling like $Ra^{0.31}$ when the optimal Γ is chosen to maximize Nu at each Ra . The measured exponent 0.31 is unlikely to be exact, so it remains possible that the asymptotic scaling of optimal- Γ steady rolls is $Nu = \mathcal{O}(Ra^{1/3})$ in the no-slip case, as in the stress-free case.

Steady rolls in the stress-free and no-slip cases differ also in their dependence on the Prandtl number. Only with stress-free boundaries do the Nusselt number Nu and Péclet number $RePr$ apparently become uniform in Pr as $Ra \rightarrow \infty$. To see how this Pr -independence emerges in the stress-free scenario, first note that area-integrated work by the buoyancy forces must balance area-integrated viscous dissipation—i.e., $Ra \langle wT \rangle = \langle |\nabla u|^2 + |\nabla w|^2 \rangle$ in the dimensionless formulation of (2.4) and (2.5). The former integral is dominated by plumes since the roll’s core is isothermal, so it scales proportionally to the dimensional quantity $\alpha \Delta g \delta h U_{rms}$, where δ is the dimensional plume thickness. The latter integral is dominated by the core since the vorticity is $\mathcal{O}(U_{rms}/h)$ everywhere in the stress-free case, so this integral scales proportionally to the dimensional quantity $\nu (U_{rms}/h)^2 h^2$. Balancing advection with diffusion of temperature anomalies in the thermal boundary layers, which also have thickness δ , requires that U_{rms} scale in proportion to $\kappa h / \delta^2$. Combining this scaling relationship with that from the integral

balance gives the dimensionless thermal boundary layer thickness as $\delta/h = \mathcal{O}(Ra^{-1/3})$ —and so $Nu = \mathcal{O}(Ra^{-1/3})$ —uniformly in Pr . These relationships also imply that U_{rms} is proportional to $(\kappa/h)Ra^{2/3}$, and so the Péclet number $RePr = U_{rms}h/\kappa$ scales as $Ra^{2/3}$ uniformly in Pr . Ultimately, it is the passivity of the vorticity boundary layers that results in the Pr -independence of these emergent bulk quantities. The vorticity layers not only make no contribution to the total dissipation at leading order, they also have no leading-order effect on the stream function that is responsible for the convective flux $\langle wT \rangle$.

The $Re = \mathcal{O}(Ra^{2/3})$ scaling found at large Ra for steady rolls and approximately evidenced in the DNS of Wang *et al.* (2020) means that buoyancy forces can sustain substantially faster-than-free-fall velocities. Indeed, if flow speeds were limited by the maximum buoyancy acceleration acting across the layer height then dimensional characteristic velocities could not be of larger order than $\sqrt{g\alpha\Delta h}$, and Re could not be larger than $\mathcal{O}(Ra^{1/2})$. Such Re may be expected if the bulk flow were dominated by effectively independent rising and falling plumes. Significantly higher speeds apparently persist within coherent convection rolls, whether steady or unsteady.

Although steady rolls cannot give heat transport larger than $Nu = \mathcal{O}(Ra^{1/3})$ as $Ra \rightarrow \infty$ in the stress-free case (Chini & Cox 2009), it is an open question whether larger Nu can result from time-dependent flows or other types of steady states in either 2D or 3D. Rigorous upper bounds on Nu derived from the governing equations—bounds depending on Ra that apply to all flows regardless of whether they are steady or unsteady and stable or unstable—do not rule out Nu growing faster than $Ra^{1/3}$. Specifically, for the 2D stress-free case Whitehead & Doering (2011) proved analytically that $Nu \leq 0.289 Ra^{5/12}$ uniformly in both Pr and domain aspect ratio. Wen *et al.* (2015a) improved the prefactor of this bound by solving the relevant variational problem numerically, computing bounds up to large finite Ra with a prefactor depending weakly on Γ . The numerical upper bound they computed for $\Gamma = 2\sqrt{2}$ is shown in figure 6; its scaling at large Ra is $Nu \leq 0.106 Ra^{5/12}$. For 3D flows in the stress-free case only the larger upper bound $Nu \leq \mathcal{O}(Ra^{1/2})$ has been proved (Doering & Constantin 1996). It remains to be seen whether upper bounds smaller than $\mathcal{O}(Ra^{5/12})$ or $\mathcal{O}(Ra^{1/2})$ can be proved for 2D or 3D flows, respectively, and whether there exists any sequence of solutions for which Nu grows faster than $\mathcal{O}(Ra^{1/3})$. In view of available evidence it is possible that, at each Ra and Pr , the steady 2D roll with the largest value of Nu —i.e., with Nu maximized over Γ —transports more heat than any other 2D or 3D solution. We are aware of no counterexamples to this possibility, either in the stress-free case studied here or in the no-slip case.

Acknowledgements

We thank L.M. Smith, D. Sondak and F. Waleffe for helpful discussions. This research was supported in part by US National Science Foundation awards DMS-1515161 and DMS-1813003, Canadian NSERC Discovery Grants Program awards RGPIN-2018-04263, RGPAS-2018-522657 and DGEGR-2018-00371, and computational resources and services provided by Advanced Research Computing at the University of Michigan.

Declaration of interests

The authors report no conflict of interest.

Appendix A. Asymptotic calculation of $RePr/Ra^{2/3}$

In this Appendix we derive the asymptotic scaling relation for Re that follows from the asymptotic analysis of Chini & Cox (2009) but is not reported there. In the large- Ra limit, a steady roll’s velocity field is properly scaled by $(\kappa/h)Ra^{2/3}$ rather than by the thermal diffusion velocity κ/h . Accordingly, we introduce the rescaled dimensionless velocity (u_∞, w_∞) , which is related to the dimensionless velocity in (2.1) by $(u, w) = Ra^{2/3}(u_\infty, w_\infty)$. With this rescaling, the expression (2.6) for Re becomes

$$Re = \frac{1}{Pr} \langle u_\infty^2 + w_\infty^2 \rangle^{1/2} Ra^{2/3} = \frac{1}{Pr} \langle |\nabla\psi_\infty|^2 \rangle^{1/2} Ra^{2/3}, \quad (\text{A } 1)$$

where ψ_∞ is the correspondingly rescaled stream function. Consequently, the prefactor in the asymptotic relation (3.1) for Re satisfies

$$c_r = \langle |\nabla\psi_\infty|^2 \rangle^{1/2}. \quad (\text{A } 2)$$

To evaluate the right-hand side of (A 2) in $Ra \rightarrow \infty$ limit we first integrate by parts to find

$$\int_0^1 \int_0^{\pi/k} |\nabla\psi_\infty|^2 dx dz = \left| \int_0^1 \int_0^{\pi/k} \psi_\infty \omega_\infty dx dz \right| \sim \Omega_c(k) \left| \int_0^1 \int_0^{\pi/k} \psi_\infty(x, z) dx dz \right|, \quad (\text{A } 3)$$

where $\nabla^2\psi_\infty = -\omega_\infty$. The asymptotic approximation in (A 3) follows from two asymptotic estimates. First, the vorticity $\omega_\infty(x, z)$ in a steady roll’s core is homogenized to a spatially uniform value Ω_c as $Ra \rightarrow \infty$, and according to the analysis of Chini & Cox this value is related the prefactor in the Nu – Ra asymptotic relation via $\Omega_c \sim \sqrt{c_n(k)}$. Second, owing to the stress-free conditions and symmetries on a steady roll’s periphery, the vorticity field is of the same asymptotic order in both the vorticity boundary layers and the core, so the contribution of these boundary layers to the middle integral in (A 3) is negligible relative to that from the $O(1)$ core where $\omega_\infty \sim \Omega_c$.

Unlike the temperature and vorticity fields, the stream function ψ_∞ at leading order in Ra is a smooth function over the entire spatial domain. The leading order expression for ψ_∞ given by equations (22)–(23) of Chini & Cox is, in our notation,

$$\psi_\infty(x, z) \sim \sum_{n=1, \text{ odd}}^{\infty} \psi_n(z) \sin(nkx) = \sum_{n=1, \text{ odd}}^{\infty} \frac{4\Omega_c}{\pi k^2 n^3} \left[1 - \frac{\cosh(nk(z - 1/2))}{\cosh(nk/2)} \right] \sin(nkx). \quad (\text{A } 4)$$

Substituting (A 4) into the right-hand side of (A 3), integrating term-by-term, dividing by the cell width π/k to obtain the spatial average, and taking the square root of the resulting expression gives the asymptotic prediction

$$c_r(k) \sim \left(\frac{8c_n(k)}{\pi^2 k^2} \sum_{n=1, \text{ odd}}^{\infty} \frac{1}{n^4} \left[1 - \frac{2 \tanh(nk/2)}{nk} \right] \right)^{1/2}. \quad (\text{A } 5)$$

Values of $c_n(k)$ and corresponding values of $c_r(k)$ for various $k \in [1/4, 10]$ are given in Table S1 of the Supplementary Material.

Supplementary Material

Table S1 gives numerical values of the asymptotic prefactors in expression (3.1) for the steady rolls constructed in the asymptotic analysis of Chini & Cox (2009). Tables S2 and S3 give the Nu and $RePr$ values plotted in figure 2. Table S4 compares steady rolls to unsteady rolls with the same mean aspect ratio from the DNS of Wang *et al.* (2020).

Figure S1 shows the normalized dissipation profiles $\bar{\varepsilon}(z)/\langle\varepsilon\rangle$ of steady rolls at various Pr for Ra values of 5×10^6 and 10^9 . There is much less variation with Pr at the larger Ra value, reflecting the Pr -independence that is predicted in the $Ra \rightarrow \infty$ asymptotic limit. Only the $Pr = 100$ profile is significantly different from the others when $Ra = 10^9$; convergence to asymptotic behaviour as $Ra \rightarrow \infty$ is slower at larger Pr (cf. figure 1).

$k = 2\pi/\Gamma$	$c_n(k)$	$c_r(k)$	$k = 2\pi/\Gamma$	$c_n(k)$	$c_r(k)$
0.25	0.09084366	0.08479653	5.25	0.26516638	0.07042333
0.5	0.13783563	0.10165665	5.5	0.26383550	0.06791123
0.75	0.17242486	0.11048428	5.75	0.26253039	0.06554476
1	0.19909232	0.11516486	6	0.26126222	0.06331554
1.25	0.21981992	0.11716681	6.25	0.26003730	0.06121496
1.5	0.23579393	0.11727251	6.5	0.25886080	0.05923472
1.75	0.24788488	0.11600002	6.75	0.25773340	0.05736652
2	0.25681088	0.11373790	7	0.25665667	0.05560274
2.25	0.26318917	0.11079160	7.25	0.25563005	0.05393607
2.5	0.26754979	0.10740171	7.5	0.25465196	0.05235964
2.75	0.27033921	0.10375413	7.75	0.25372157	0.05086718
3	0.27192661	0.09998906	8	0.25283657	0.04945277
3.25	0.27260954	0.09620876	8.25	0.25199552	0.04811103
3.5	0.27262477	0.09248559	8.5	0.25119483	0.04683679
3.75	0.27215669	0.08886847	8.75	0.25043350	0.04562556
4	0.27134834	0.08538889	9	0.24970964	0.04447307
4.25	0.27030747	0.08206516	9.25	0.24902004	0.04337532
4.5	0.26911578	0.07890636	9.5	0.24836456	0.04232885
4.75	0.26783386	0.07591494	9.75	0.24773960	0.04133018
5	0.26650668	0.07308893	10	0.24714363	0.04037628

Table S1: Numerical values of the asymptotic prefactors c_n and c_r in (3.1) for various wavenumbers k . Values of c_n are from the data of Chini & Cox (2009), and c_r is calculated from c_n according to (A 5).

Ra	$N_x \times N_z$	Nu				
		$Pr = 10^{-2}$	$Pr = 10^{-1}$	$Pr = 1$	$Pr = 10$	$Pr = 10^2$
10^3	128×65	1.46630	1.46614	1.46687	1.46716	1.46718
$10^{13/4}$	128×65	2.37255	2.37025	2.36637	2.37324	2.37425
$10^{14/4}$	128×65	3.18564	3.18049	3.15193	3.16265	3.16748
$10^{15/4}$	128×65	4.05203	4.04468	3.98471	3.96052	3.97220
10^4	128×65	5.07914	5.07051	4.98831	4.86435	4.88129
$10^{17/4}$	128×65	6.32515	6.31587	6.22172	5.94155	5.94945
$10^{18/4}$	128×65	7.83124	7.82158	7.72035	7.25591	7.21592
$10^{19/4}$	128×65	9.65227	9.64234	9.53590	8.89159	8.72489
10^5	128×65	11.8568	11.8467	11.7360	10.9457	10.5267
$10^{21/4}$	256×97	14.5268	14.5164	14.4021	13.5059	12.6816
$10^{22/4}$	256×97	17.7612	17.7506	17.6329	16.6557	15.2701
$10^{23/4}$	256×97	21.6798	21.6690	21.5483	20.5044	18.4060
10^6	256×97	26.4274	26.4164	26.2929	25.1935	22.2598
$10^{25/4}$	256×97	32.1797	32.1685	32.0425	30.8962	27.0879
$10^{26/4}$	256×97	39.1494	39.1379	39.0094	37.8234	33.2279
$10^{27/4}$	512×129	47.5938	47.5822	47.4514	46.2312	41.0104
10^7	512×129	57.8250	57.8132	57.6802	56.4307	50.7115
$10^{29/4}$	512×129	70.2211	70.2091	70.0740	68.7989	62.6608
$10^{30/4}$	512×129	85.2397	85.2277	85.0905	83.7928	77.2962
$10^{31/4}$	512×129	103.437	103.424	103.285	101.967	95.1593
10^8	512×129	125.484	125.472	125.330	123.991	116.909
$10^{33/4}$	768×193	152.192	152.179	152.036	150.683	143.355
$10^{34/4}$	1024×193	184.554	184.541	184.394	183.026	175.477
$10^{35/4}$	1024×257	223.758	223.745	223.599	222.215	214.465
10^9	1024×257	271.266	271.253	271.105	269.698	261.773
$10^{37/4}$	1280×257		328.798	328.713	327.238	319.134
$10^{38/4}$	1280×257		398.523	398.427	397.003	388.734
$10^{39/4}$	1536×257		483.062	482.910	481.470	473.049
10^{10}	1792×257		585.437	585.285	583.841	575.311
$10^{41/4}$	2048×321				707.958	699.254
$10^{42/4}$	2560×321				858.111	849.325
$10^{43/4}$	3072×321				1040.21	1031.35
10^{11}	3584×321					1251.98

Table S2: Values of the Nusselt number (Nu) plotted in figure 2(a) for steady rolls of aspect ratio $\Gamma = 2$ ($k = \pi$). The resolution of Fourier modes (N_x) and Chebyshev collocation points (N_z) is given also.

Ra	$N_x \times N_z$	$RePr$				
		$Pr = 10^{-2}$	$Pr = 10^{-1}$	$Pr = 1$	$Pr = 10$	$Pr = 10^2$
10^3	128×65	4.860211	4.859365	4.863013	4.864534	4.864669
$10^{13/4}$	128×65	11.11289	11.10342	11.08274	11.10817	11.11225
$10^{14/4}$	128×65	18.64998	18.62765	18.48547	18.50202	18.52133
$10^{15/4}$	128×65	29.18438	29.14861	28.81749	28.56985	28.61439
10^4	128×65	44.44510	44.39718	43.87005	42.81088	42.85149
$10^{17/4}$	128×65	66.65392	66.59490	65.87916	63.22068	63.10225
$10^{18/4}$	128×65	99.00479	98.93476	98.02324	92.79036	92.04534
$10^{19/4}$	128×65	146.2211	146.1395	145.0123	136.1512	133.5699
10^5	128×65	215.2057	215.1114	213.7389	200.3372	193.1899
$10^{21/4}$	256×97	316.0649	315.9563	314.2983	295.6302	278.8445
$10^{22/4}$	256×97	463.6093	463.4841	461.4878	436.6766	402.1873
$10^{23/4}$	256×97	679.5490	679.4041	677.0022	644.8536	580.6680
10^6	256×97	995.7158	995.5474	992.6546	951.6627	841.1621
$10^{25/4}$	256×97	1458.790	1458.594	1455.104	1403.377	1226.322
$10^{26/4}$	256×97	2137.241	2137.009	2132.789	2067.960	1803.793
$10^{27/4}$	512×129	3131.499	3131.224	3126.109	3045.229	2674.566
10^7	512×129	4588.895	4588.574	4582.361	4481.765	3981.512
$10^{29/4}$	512×129	6725.606	6725.221	6717.660	6592.805	5932.137
$10^{30/4}$	512×129	9858.786	9858.334	9849.112	9694.374	8833.901
$10^{31/4}$	512×129	14453.85	14453.31	14442.05	14250.46	13140.24
10^8	512×129	21193.84	21193.21	21179.44	20942.25	19519.46
$10^{33/4}$	768×193	31080.45	31079.68	31062.85	30769.81	28954.88
$10^{34/4}$	1024×193	45585.16	45584.26	45563.33	45201.19	42895.45
$10^{35/4}$	1024×257	66865.43	66864.32	66839.10	66391.72	63471.97
10^9	1024×257	98091.13	98089.85	98058.98	97504.78	93819.57
$10^{37/4}$	1280×257		143906.3	143882.5	143186.5	138542.0
$10^{38/4}$	1280×257		211139.3	211107.6	210266.2	204428.0
$10^{39/4}$	1536×257		309825.2	309769.0	308731.1	301407.4
10^{10}	1792×257		454641.9	454573.4	453293.9	444122.9
$10^{41/4}$	2048×321				665545.3	654078.8
$10^{42/4}$	2560×321				977028.2	962715.7
$10^{43/4}$	3072×321				1434327	1416484
10^{11}	3584×321					2083475

Table S3: Values of the Péclet number ($RePr$) plotted in figure 2(b) for steady rolls of aspect ratio $\Gamma = 2$ ($k = \pi$). The resolution of Fourier modes (N_x) and Chebyshev collocation points (N_z) is given also.

Ra	Steady roll		DNS	
	Nu	Re	Nu	Re
10^7	53.2089	515.276	48.53	488.77
3×10^7	77.5286	1080.31	69.43	1016.46
10^8	116.711	2425.10	96.81	2202.08
3×10^8	169.146	5063.63	134.00	4552.41
10^9	253.606	11332.6	198.01	10135.1

Table S4: Comparison of Nu and Re between steady rolls with fixed aspect ratio $\Gamma = 3.2$ and unsteady DNS by Wang *et al.* (2020) with the same mean aspect ratio. In both cases $Pr = 10$.

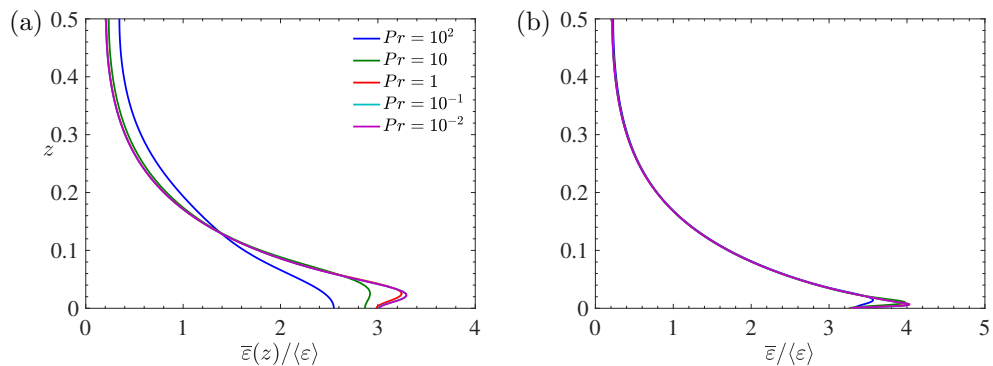


Figure S1: Horizontally averaged dissipation profiles normalized by their volume averages, $\bar{\epsilon}(z)/\langle\epsilon\rangle$, for steady convective rolls at (a) $Ra = 5 \times 10^6$ and (b) $Ra = 10^9$ with $\Gamma = 2$ and various Pr . Only half of the vertical domain is shown ($0 \leq z \leq 0.5$) because the profiles are symmetric about the mid-plane.

REFERENCES

- CHILLÀ, FRANCESCA & SCHUMACHER, JOERG 2012 New perspectives in turbulent Rayleigh–Bénard convection. *The European Physical Journal E* **35** (7), 1–25.
- CHINI, G.P. & COX, S.M. 2009 Large Rayleigh number thermal convection: Heat flux predictions and strongly nonlinear solutions. *Physics of Fluids* **21**, 083603.
- DOERING, C.R. 2020 Turning up the heat in turbulent thermal convection. *Proceedings of the National Academy of Sciences* **117**, 9671–9673.
- DOERING, C. R. & CONSTANTIN, P. 1996 Variational bounds on energy dissipation in incompressible flows. III. Convection. *Phys. Rev. E* **53**, 5957–5981.
- GOLUSKIN, D. 2015 *Internally heated convection and Rayleigh–Bénard convection*. Springer.
- GOLUSKIN, D., JOHNSTON, H., FLIERL, G.R. & SPIEGEL, E.A. 2014 Convectively driven shear and decreased heat flux. *Journal of Fluid Mechanics* **759**, 360–385.
- KADANOFF, L.P. 2001 Turbulent heat flow: Structures and scaling. *Physics Today* **54**, 34–39.
- LORENZ, E.N. 1963 Deterministic nonperiodic flow. *Journal of the Atmospheric Sciences* **20**, 130–141.
- MALKUS, W.V.R. & VERONIS, G. 1958 Finite amplitude cellular convection. *Journal of Fluid Mechanics* **4**, 225–260.
- NEWELL, A.C. & WHITEHEAD, J.A. 1969 Finite bandwidth, finite amplitude convection. *Journal of Fluid Mechanics* **38**, 279–303.
- PANDEY, A., VERMA, M.K. & MISHRA, P.K. 2014 Scaling of heat flux and energy spectrum for very large Prandtl number convection. *Physical Review E* **89**, 023006.
- PANDEY, A. & VERMA, M. K. 2016 Scaling of large-scale quantities in Rayleigh–Bénard convection. *Physics of Fluids* **28**, 095105.
- PANDEY, A., VERMA, M. K., CHATTERJEE, A. G. & DUTTA, B. 2016 Similarities between 2D and 3D convection for large Prandtl number. *Pramana – J. Phys.* **87**, 13.
- PAUL, S., VERMA, M. K., WAHI, P., REDDY, S. K. & KUMAR, K. 2012 Bifurcation analysis of the flow patterns in two-dimensional Rayleigh–Bénard convection. *Int. J. Bifurc. Chaos* **22**, 1230018.
- PETSCHEL, K., STELLMACH, S., WILCZEK, M., LÜLFF, J. & HANSEN, U. 2013 Dissipation layers in Rayleigh–Bénard convection: A unifying view. *Physical Review Letters* **110**, 114502.
- VAN DER POEL, E.P., OSTILLA-MÓNICO, R., VERZICCO, R. & LOHSE, D. 2014 Effect of velocity boundary conditions on the heat transfer and flow topology in two-dimensional Rayleigh–Bénard convection. *Physical Review E* **90**, 013017.
- RAYLEIGH, LORD 1916 On convection currents in a horizontal layer of fluid, when the higher temperature is on the under side. *Philosophical Magazine* **32**, 529–546.
- ROBINSON, J.L. 1967 Finite amplitude convection cells. *Journal of Fluid Mechanics* **30**, 577–600.
- SONDAK, D., SMITH, L.M. & WALEFFE, F. 2015 Optimal heat transport solutions for Rayleigh–Bénard convection. *Journal of Fluid Mechanics* **784**, 565–595.
- TREFETHEN, L.N. 2000 *Spectral Methods in MATLAB*. SIAM.
- TREFETHEN, L.N. & BAU III, D. 1997 *Numerical Linear Algebra*. Philadelphia: SIAM.
- WALEFFE, F., BOONKASAME, A. & SMITH, L.M. 2015 Heat transport by coherent Rayleigh–Bénard convection. *Physics of Fluids* **27**, 051702.
- WANG, Q., CHONG, K.-L., STEVENS, R.J.A.M., VERZICCO, R. & LOHSE, D. 2020 From zonal flow to convection rolls in Rayleigh–Bénard convection with free-slip plates. *arXiv:2005.02084* .
- WEN, B. & CHINI, G.P. 2018 Inclined porous medium convection at large Rayleigh number. *Journal of Fluid Mechanics* **837**, 670–702.
- WEN, B., CHINI, G.P., KERSWELL, R.R. & DOERING, C.R. 2015a Time-stepping approach for solving upper-bound problems: Application to two-dimensional Rayleigh–Bénard convection. *Physical Review E* **92**, 043012.
- WEN, B., CORSON, L.T. & CHINI, G.P. 2015b Structure and stability of steady porous medium convection at large Rayleigh number. *Journal of Fluid Mechanics* **772**, 197–224.
- WHITEHEAD, J.P. & DOERING, C.R. 2011 Ultimate state of two-dimensional Rayleigh–Bénard convection between free-slip fixed-temperature boundaries. *Physical Review Letters* **106**, 244501.